Supporting Information

Aggregation kinetics of the Aβ1-40 peptide monitored by NMR

Giovanni Bellomo,[a] Sara Bologna,[a] Leonardo Gonnelli,[a] Enrico Ravera,[a,b] Marco Fragai, [a,b] Moreno Lelli,[a,b,*] and Claudio Luchinat [a,b,*]

[a.] *Magnetic Resonance Center (CERM), University of Florence, Via L. Sacconi 6, 50019 Sesto Fiorentino, Italy.*
[b.] *Department of Chemistry "Ugo Schiff", University of Florence, Via della Lastruccia 3, 50019 Sesto Fiorentino, Italy.*
[c.] *Giotto Biotech S.R.L., Via Madonna del Piano 6, 50019 Sesto Fiorentino, Florence, Italy*
**To whom correspondence should be addressed*

Contents

1. 1D ^{1}H NMR experiments to monitor kinetics

The NMR investigation was performed on Aβ1-40 samples at pH 8.5 and with concentrations between 30 and 100 µM. This higher than physiological pH was chosen because it corresponds to the pH where Aβ1-40 easily form fibrils with high reproducibility.[1] Most of the analyses were performed on 1D ^{1}H NMR spectra. 1D spectra were preferred compared to 2D because they provide a higher signal-to-noise ratio for the same amount of time. Figure S1 shows the methyl region of the 1D ^{1}H NMR spectrum of Aβ1-40 acquired at 50 µM, at 310 K and at different times (t). It can be seen that during aggregation the protein signals decay without the growth of any new visible peak or change in the pattern profile: in Figure S1B it is possible to appreciate that the spectrum after 33.2 h maintains the same profile of the monomeric spectrum acquired at 0.66 h with some small differences around 0.95 ppm (that accounts less than 2% of methyl protons starting integral), due to the rescaled signals of protease inhibitors added to prevent protein degradation (see details below, in the Experimental session). We decided to compare our NMR integrals with the simulated monomer concentration (estimated by kinetic models) because we had no hints (no new growing peaks in the 1D NMR spectra) about any contribution from other species in the integration regions we considered, up to 80 h of aggregation.

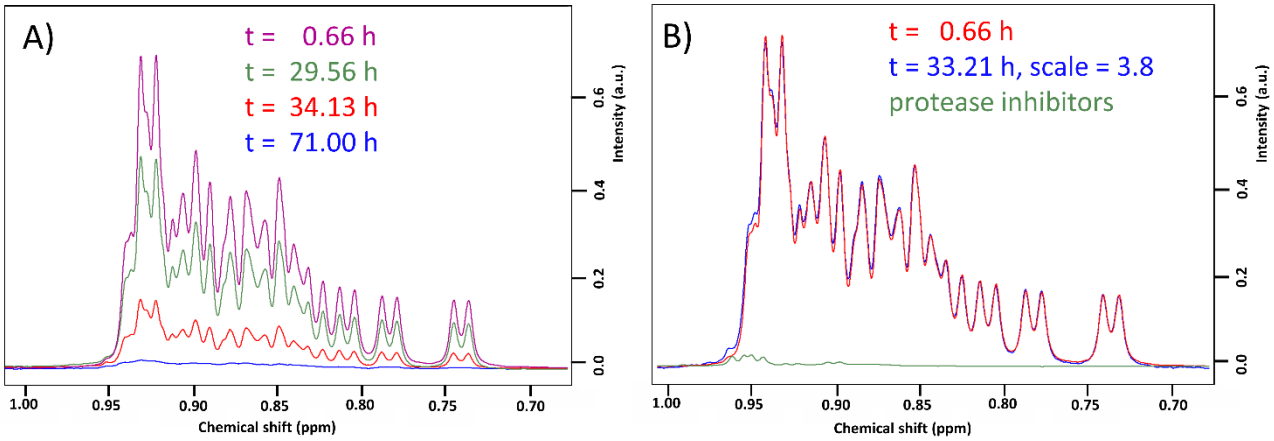

Figure S1: A) Decay of the monomer methyl signals from 1D ^{1}H NMR experiments acquired in a 700 MHz spectrometer. Line broadening was set to 1.0 Hz. The Aβ1-40 monomer starting concentration was 50 µM in ammonium acetate buffer, pH 8.5 and T = 310 K. B) Superposition of the methyl signal at 0.66h (red) with those at 33.21h rescaled (x3.8, blue). The methyl signals retain their shape during aggregation, indicating that species with a spectrum different from monomer are almost not visible by 1D ^{1}H NMR in this spectra region and in our experimental conditions. The only differences between the monomer and the rescaled spectrum, at t = 33 h, can be found at 0.95 ppm where small signals from protease inhibitors are present.

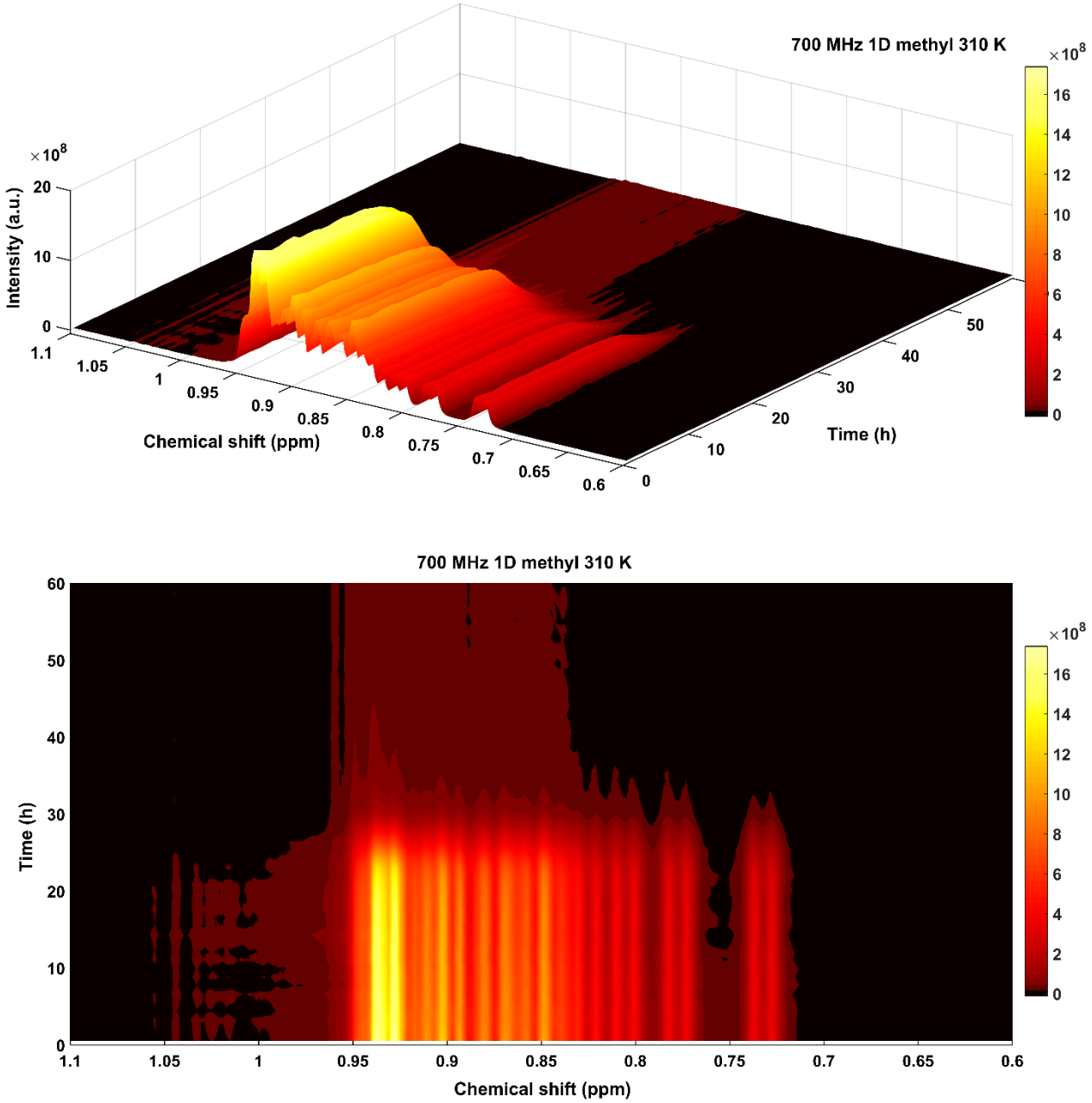

Figure S2: Series of 1D ^{1}H NMR spectra of the methyl region of a 50 µM sample of Aβ1-40 plotted in two different projections (graphical image produced with MATLAB R2017a). Spectra were acquired in a 700 MHz (16.4 T) spectrometer, using an ammonium acetate buffer with 0.2% of sodium azide, 1.0 mM EDTA and protease inhibitors at low concentrations (the ABSF was 10 µM, see Experimental for details). Spectra were binned (bin width = 0.005 ppm) with AMIX (Analysis of MIXtures software, Bruker Biospin) prior to image formation.

In addition to the methyl spectral region, also the aromatic resonances were analysed with very little interference from the background. On these signals, the 1D-NOESY spectra performed better than the 1D ^{1}H excitation sculpting experiments, because the water pre-saturation steps strongly attenuated the buffer resonances in exchange with water (i.e. ammonium and ammonia).

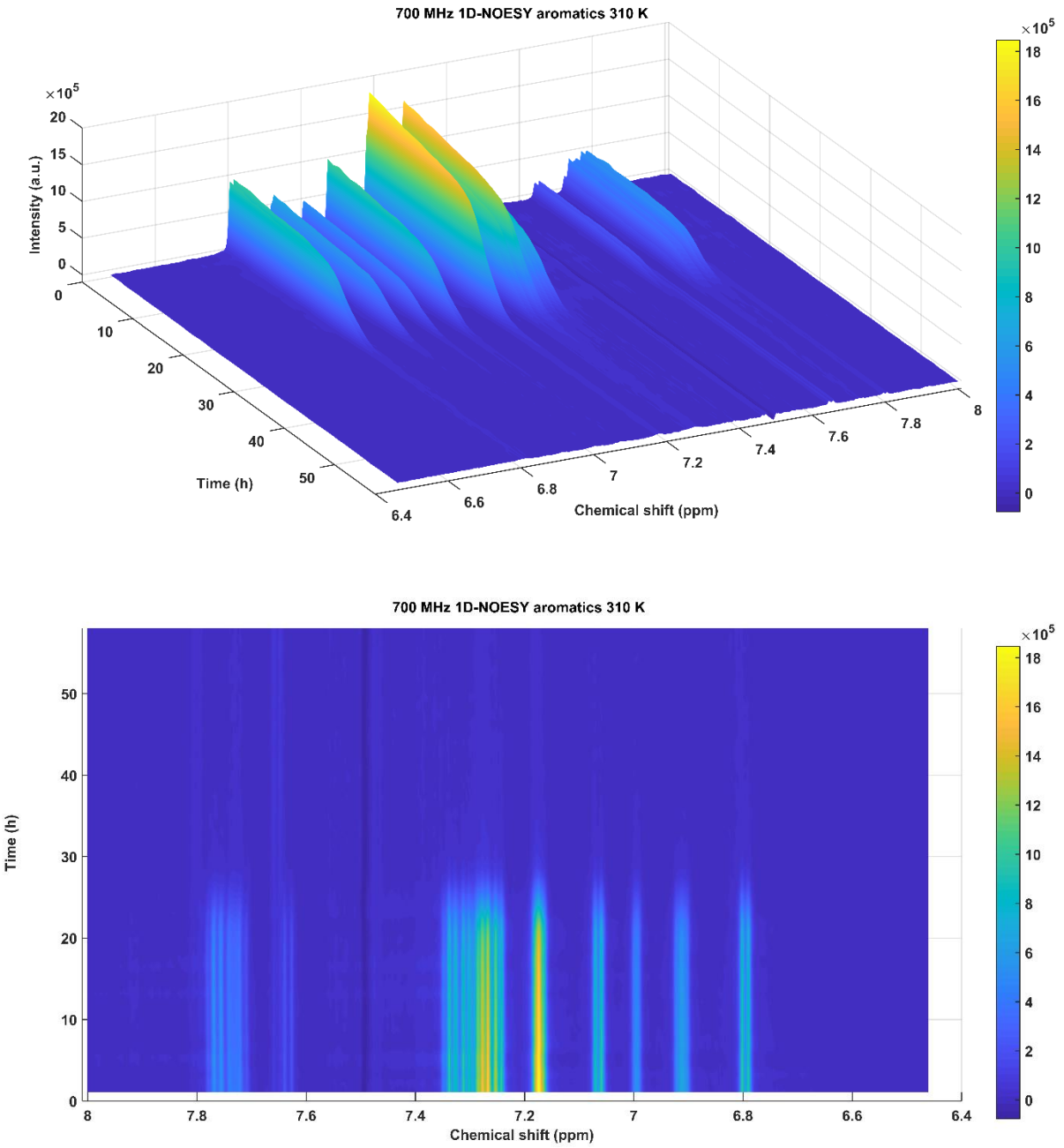

Figure S3: Series of 1D ^{1}H-NOESY spectra of the aromatic region of a 50 µM sample of Aβ1-40 plotted in two different projections, from one side (upper panel) and from the top(lower panel) (graphical image produced with MATLAB R2017a). Spectra were acquired in a 700 MHz (16.4 T) spectrometer, using an ammonium acetate buffer with 0.2% of sodium azide, 1.0 mM EDTA and protease inhibitors at low concentrations (the ABSF was 10 µM, see Experimental Session for details). Spectra were binned (bin width = 0.005 ppm) with AMIX (Analysis of MIXtures software, Bruker Biospin) prior to image formation.

2. Kinetic models

In the model we tested in this work (depicted graphically in Fig. S4 and mathematically in Eq. S1 and S2), monomers can nucleate into oligomers, the nucleation kinetics we considered is fundamentally equal to the one used by Knowles,[2] Ferrone,[3] Pöschel[4] and to the one originally developed by Oosawa.[5] In our case, however, monomers do not nucleate directly into fibrils but into a transient, on pathway oligomeric aggregates. Oligomers can grow and decrease by addition or dissociation of monomers, as well as fibrils, but with different

kinetic rates with respect to the latter. For the growth kinetics of oligomers we applied the same mathematical description of Knowles,[2] Ferrone,[3] Pöschel[4] and Oosawa,[5] while for the depolymerization kinetics we used slightly different terms in the kinetic equations: since oligomers are generally species less stable than fibrils, the overall dissociation rate of a single peptide is likely not the same for any oligomer and we scaled it for the larger monomer content in the aggregate, resulting in a total probability of detachment proportional to the oligomer size. The crucial part of the model is the introduction of a conversion kinetics step from oligomers to fibrils: when the oligomers reach a given critical size n_c (e.g. 20 monomers in the present case) they are allowed to irreversibly convert into fibrils. Fibrils can then grow and decrease through polymerization and depolymerization by addition or release of Aβ1-40 monomers. The mathematical description of the polymerization and depolymerization of fibrils is identical to the one of the cited models.[3–7] Fibrils can then also fragment producing smaller fibrils that can then act as new seeds for polymerization. In this model fibrils are not allowed to fragment in species smaller than the critical size n_c, in this way fragmentation of fibrils only produces fibrils above the critical size and this is why we dubbed this process "fibril closed fragmentation". With this constraint we wanted to force the fibrillary "nuclei" converted from oligomers to be stable and to be only subjected to depolymerization. The mathematical description of the model is reported in Eq. S1 and Eq. S2 in the master equation formalism. We report as fi and Oi the fibrils and oligomers populations made by i monomers, respectively. θ is the Heaviside theta function, δ is the Dirac delta function, n0 is the minimum nucleus size, nc is the critical size for oligomer conversion into fibrils, m is the Aβ1-40 monomer population. The values of the k constants reflect the importance of the corresponding process (the colour code in Eq. S1 and S2 matches the one in Fig. S4).

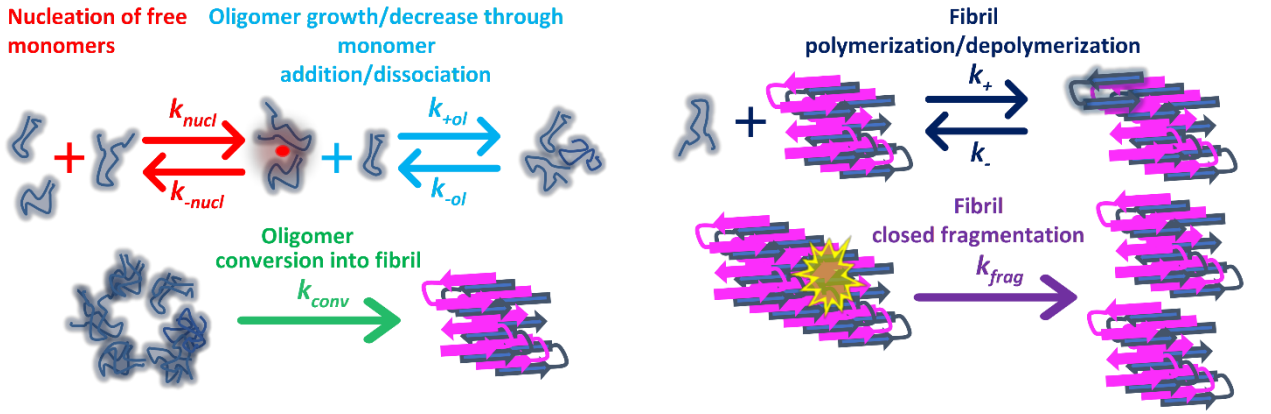

Figure S4: Schematic description of the developed kinetic model for the aggregation of Aβ1-40. The colors of the processes names correspond to the colors of the terms descriptive of the model in Eq. S1 and Eq. S2.

$$\frac{df_i}{dt} = +k_{conv}O_i\theta(i-n_c) - k_+f_i m + k_+f_{i-1}m - k_-f_i + k_-f_{i+1} - k_{frag}(i-2n_c+1)f_i\theta(i-2n_c) + 2k_{frag}\sum_{j=i+n_c}^{\infty} f_j \qquad \text{(S1)}$$

$$\frac{dO_i}{dt} = +k_{nucl}\delta(i-n_0)m^{n_0} - k_{-nucl}\delta(i-n_0)n_0O_{n_0} - k_{+ol}O_i m + k_{+ol}O_{i-1}m - k_{-ol}iO_i\theta(i-n_0) +$$

$$+k_{-ol}(i+1)O_{i+1}\theta(i-n_0+1) - k_{conv}O_i\theta(i-n_c) \qquad \text{(S2)}$$

As depicted in the equations below, oligomer total population and mass are calculated by summing up all the O_i terms (Eq. S3), while the differential equations for fibril total population and mass are calculated by using the condensed expressions for the summations (Eq. S3). These condensed expressions were obtained from Eq. S1 with calculations similar to the ones performed by Pöschel et al..[4] comparing the experimental time points of monomer depletion with the simulated monomer m(t), calculated by Eq. S5 through the numerical integration of Eq. S3 and Eq. S4. In the equations below, the terms O_{Max} represent the maximum allowed size of oligomers for the numerical solving of the differential equations, theoretically this term can go up to ∞ but in our simulations oligomer population were almost empty after $i = 30$, see Fig. S8B.

$$\frac{dO}{dt} = \sum_{i=n_0}^{O_{Max}} \frac{dO_i}{dt}; \qquad \frac{dO_{crit}}{dt} = \sum_{i=n_c}^{O_{Max}} \frac{dO_i}{dt}; \qquad \frac{dM_O}{dt} = \sum_{i=n_0}^{O_{Max}} i\frac{dO_i}{dt}; \qquad \frac{dM_{O\,crit}}{dt} = \sum_{i=n_c}^{O_{Max}} i\frac{dO_i}{dt} \tag{S3}$$

$$\frac{dF}{dt} = \sum_{i=n_c}^{\infty} \frac{df_i}{dt} = k_{conv}O_{crit} + k_{frag}\left(M_f - F(2n_c+1)\right); \qquad \frac{dM_f}{dt} = \sum_{i=n_c}^{\infty} i\frac{df_i}{dt} = k_{conv}M_{O\,crit} + k_+ mF - k_- F \tag{S4}$$

$$m = m_0 - \sum_{i=n_c}^{\infty} if_i - \sum_{i=n_0}^{\infty} iO_i = m_0 - M_f - M_O \tag{S5}$$

The cumulative masses of aggregated species are defined as M_f, M_O, M_{Ocrit}, for the total mass of fibrils, oligomers and oligomers above the critical size (n_c), respectively. This new proposed model contains oligomeric intermediates with different aggregation properties and kinetic constants with respect to fibrils. We put $n_0 = 2$, we considered the smallest oligomer as the dimer and the best fit was achieved using $n_c = 20$ as critical size. In Table S1 we reported the fitted kinetic constants for this model and for the other two model considered in the main text, that one developed for the aggregation of Aβ1-42[2] and that one for Aβ1-40[8] at pH 7.4. The agreement between calculated and experimental values is now optimal also during the lag-time where the monomer concentration is decreasing due to the progressive formation of oligomeric species. In our model, the kinetic constant for the monomer addition to fibrils species (k_+) is an order of magnitude higher than the one for the monomer addition to oligomeric species (k_{+ol}). This difference explains why, once a sufficient amount of large oligomers is converted to fibrils, monomers start to be rapidly consumed while the mass of fibrils rapidly increases producing a sigmoidal behaviour for the monomer consumption kinetics. In the third part of the trend, where most of the peptides are aggregated into fibrils, the process of monomer dissociation becomes relevant and is responsible for the residual amount of monomer still present in solution in the tail of the sigmoidal decrease. The critical size of the oligomer-to-fibril conversion was found to be $n_c = 20$; this number is anyway just an estimate, since reasonably good values were found also for $15<n_c<40$, and we cannot exclude that conversion may begin at even larger sizes.

Parameters	Conversion model	Model Aβ1-40	Model Aβ1-42
k_{nucl} $[M^{-1}s^{-1}]$	$1.25\cdot10^{-6}$	$2.64\cdot10^{-10}$	$1.28\cdot10^{-9}$
k_{-nucl} $[s^{-1}]$	$6.96\cdot10^{-9}$	-	-
k_+ $[M^{-1}s^{-1}]$	$2.83\cdot10^{-1}$	$7.09\cdot10^{-3}$	$6.19\cdot10^{-4}$
k_- $[s^{-1}]$	$5.22\cdot10^{-7}$	$6.11\cdot10^{-21}$	$2.57\cdot10^{-12}$
k_{frag} $[s^{-1}]$	$8.68\cdot10^{-11}$	-	$2.52\cdot10^{-12}$
k_{nucl2} $[M^{-2}s^{-1}]$	-	1.92	6.54
k_{+ol} $[M^{-1}s^{-1}]$	$2.11E\cdot10^{-2}$	-	-
k_{-ol} $[s^{-1}]$	$1.30\cdot10^{-7}$	-	-
k_{conv} $[s^{-1}]$	$1.35\cdot10^{-8}$	-	-
K_{sat} $[M^2]$	-	$9.73\cdot10^{-5}$	-

Table S1: Fitted parameters for the conversion model developed in this work, for the Aβ1-40 model from the work of Meisl, Knowles and co-workers[8] and for the Aβ1-42 model from the works of Knowles, Dobson and co-workers.[2]

3. Test with secondary nucleation active

We repeated the fitting procedure by adding the secondary nucleation term (depicted in the line below) in Eq. S1.

$$+\delta(i-n_2)m^{n_2}\sum_{j=2}^{\infty} jf_j$$

In this term we considered the fibrillary nucleus size $n_2 = 2$, with the meaning that fibril-like dimers are allowed to form on the fibril surface of all the other fibrils. The fitting results are shown in Fig. S5 and the fitted kinetic constants are in Table S2.

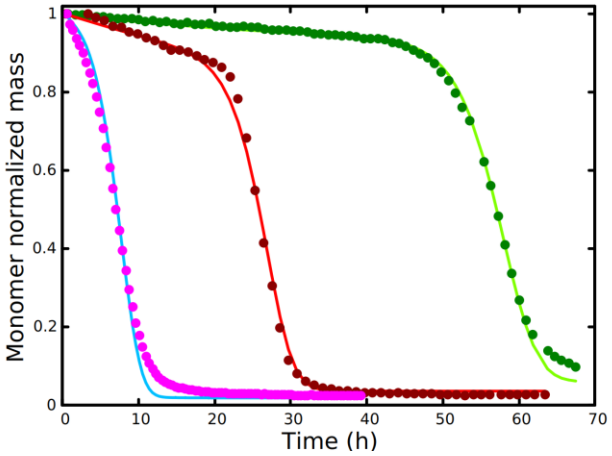

Figure S5: Simulated monomer populations coming from the "conversion" model with secondary nucleation were fitted to the experimental data coming from the integration of the methyl region of 1D solution NMR spectra at different starting monomer concentrations (30, 50 and 100 µM).

Parameters	Conversion Model with secondary nucleation
k_{nucl} $[M^{-1}s^{-1}]$	$1.23 \cdot 10^{-6}$
k_{-nucl} $[s^{-1}]$	$7.87 \cdot 10^{-9}$
k_{+} $[M^{-1}s^{-1}]$	$3.18 \cdot 10^{-1}$
k_{-} $[s^{-1}]$	$5.49 \cdot 10^{-7}$
k_{frag} $[s^{-1}]$	$7.41 \cdot 10^{-11}$
k_{nucl2} $[M^{-2}s^{-1}]$	$5.89 \cdot 10^{-6}$
k_{+ol} $[M^{-1}s^{-1}]$	$2.30 \cdot 10^{-2}$
k_{-ol} $[s^{-1}]$	$1.39 \cdot 10^{-7}$
k_{conv} $[s^{-1}]$	$1.04 \cdot 10^{-8}$

Table S2: Fitted kinetic constants for the conversion model developed in this work with secondary nucleation added. The kinetic constant relative to the secondary surface catalyzed nucleation remains quite smal (see the fitted values for the two-species models in Table 1) in order to fit the NMR data.

4. Including low molecular weight (LMW) oligomers in the fitting

In the first chapter of these Supporting Information we showed how the observed species in the 1D spectrum is essentially the monomeric peptide. Nevertheless, oligomers even up to about 10 units have a molecular weight <50 kDa and should be visible in the NMR spectrum. Thus, we cannot exclude that integrating the methyl region we can include resonances of small oligomeric species. To demonstrate the robustness of the analysis, we repeated the simulation of the oligomer-to-fibril conversion model considering as visible in the integral also LMW oligomeric species until hexamers (species until hexamers should be clearly visible by 1D NMR). We examined two cases: first we repeated the fit using the same constants of Table 1, but including in the simulated curve the LMW oligomers (Figure S6A). Second, we repeated the fit allowing the constant to be adapted (Figure S6B & Table S3). Since these small-size oligomeric species are transient and present in low concentration (at least in our simulations) taking them into account while fitting the NMR data caused only minimal differences in the trend of the calculated curves.

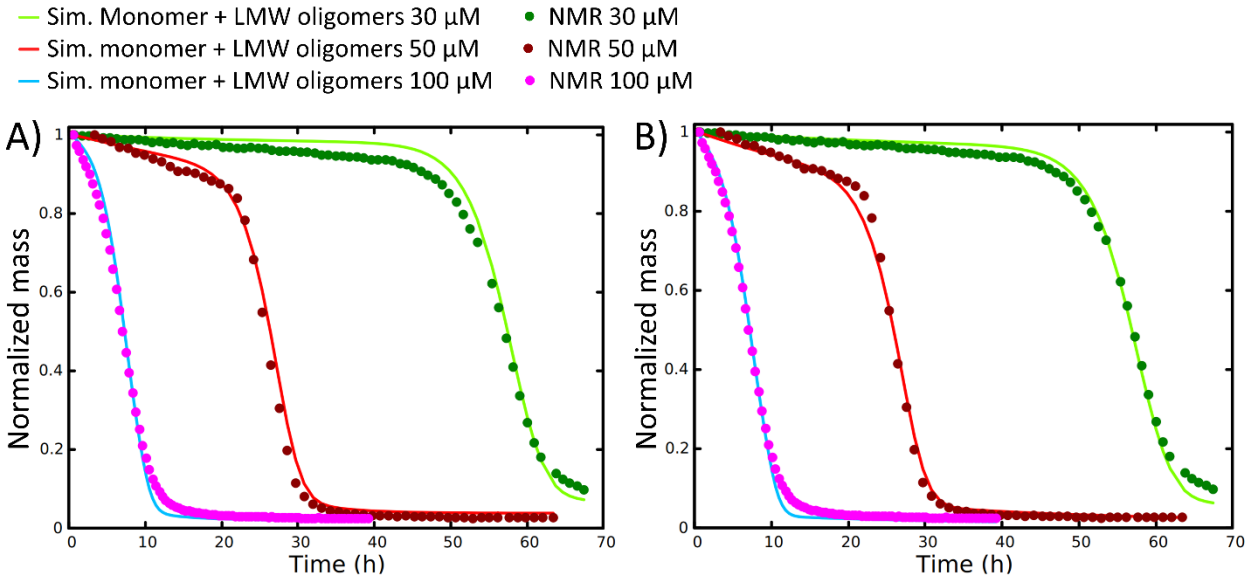

Figure S6: A) Simulated monomer and small oligomer populations (oligomers of size ≤6 and monomers were included) coming from the "conversion" model were fitted to the experimental data coming from the integration of the methyl region of 1D solution NMR spectra at different starting monomer concentrations (30, 50 and 100 µM), the kinetic constants used were the ones of Table 1. B) kinetic constants were optimized to fit monomers and species until hexamers (fitted parameters are present in Table S3).

Parameters	Conversion model with LMW oligomeric species
k_{nucl} $[M^{-1}s^{-1}]$	$1.51 \cdot 10^{-6}$
k_{-nucl} $[s^{-1}]$	$1.53 \cdot 10^{-9}$
k_{+} $[M^{-1}s^{-1}]$	$2.67 \cdot 10^{-1}$
k_{-} $[s^{-1}]$	$1.93 \cdot 10^{-7}$
k_{frag} $[s^{-1}]$	$8.50 \cdot 10^{-11}$
k_{nucl2} $[M^{-2}s^{-1}]$	-
k_{+ol} $[M^{-1}s^{-1}]$	$2.87 \cdot 10^{-2}$
k_{-ol} $[s^{-1}]$	$1.64 \cdot 10^{-7}$
k_{conv} $[s^{-1}]$	$7.32 \cdot 10^{-9}$

Table S3: kinetic constants relative to the fitted data in Figure S6 (right).

5. Populations of the aggregates

On the basis of the fitted constants of Table S1, we back-calculated the relative size of the fibril distribution for the three models (Fig. S8 and Fig. S9). With reference to Figure S7, it results that, for the Aβ1-42 and Aβ1-40 models at the end of the aggregation process of the 50 µM sample (t ~60h), the majority of the fibrils should have a size smaller than 20 monomers, and for the Aβ1-42 model even smaller than 10 monomers (40 kDa). In the trials we made, only the model based on the oligomer-to-fibril conversion predicts the formation of fibrils larger than 433 kDa (>100mers). Indeed, the strong secondary nucleation process of the first two models results in a rapid formation of nucleation seeds during the sigmoidal step that are not able to elongate much because of the depleted monomers in solution. In our conversion model we have not included the secondary nucleation process and the "limited" number of converted fibrils favors their elongation towards higher molecular weights.

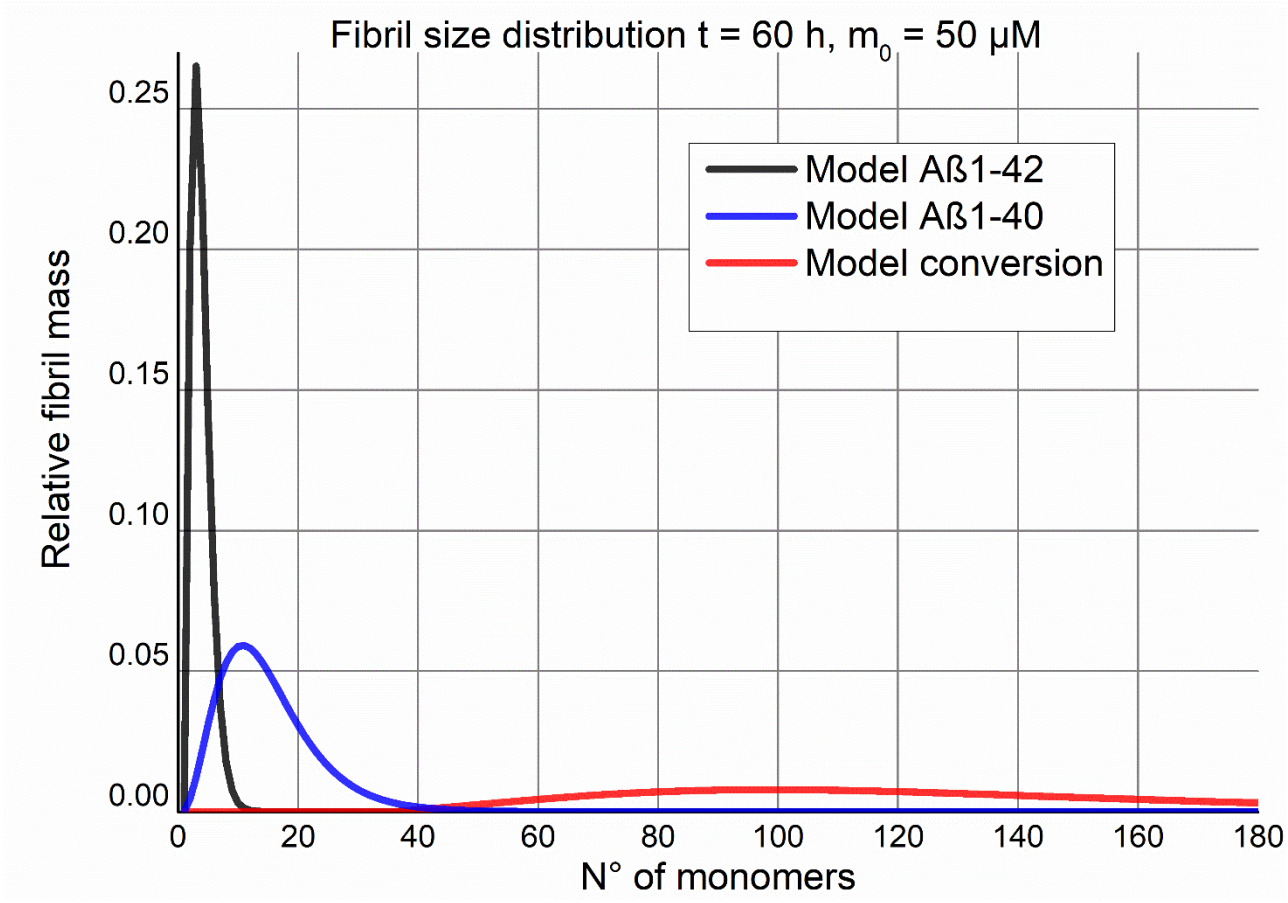

Figure S7: The distributions of the fibril size at t = 60 for the three models tested are plotted together. The model for Aβ1-42 produced a large amount of dimers through secondary nucleation in order to fit the experimental data.

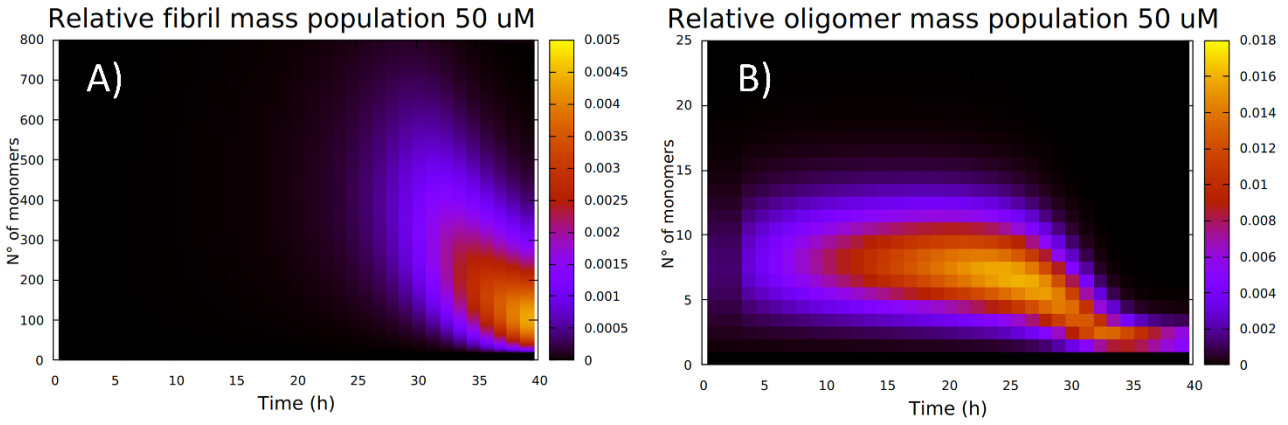

Figure S8: Size distribution of fibrillary (A) and oligomeric (B) species during the simulation of the aggregation kinetics of the 50 µM sample of Aβ1-40. The simulations are relative to the conversion model. The decay of the average size of fibrils (from ~500 peptide units to ~100) over time is caused by the fragmentation kinetics[4,9] which is not countered by any agglomeration of aggregates in this simplified model.

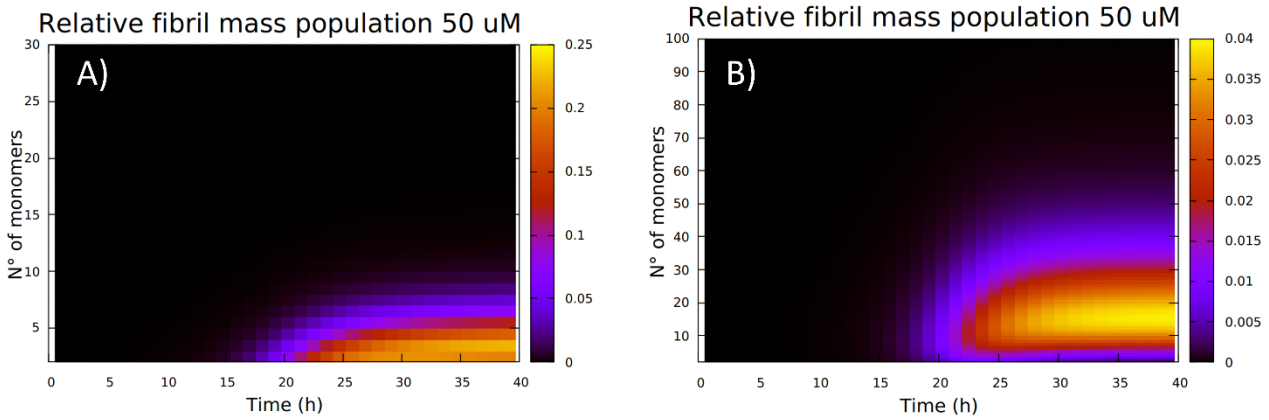

Figure S9: Size distribution of fibrillary species during the simulation of the aggregation kinetics of the 50 μM sample of Aβ1-40. In A) the simulations are relative to the model for Aβ1-42[2] while in B) are relative to the model for Aβ1-40.[8]

6. Experimental details that can affect the aggregation kinetics

The experimental investigation of the aggregation kinetics with Aβ peptides is quite challenging, since there are many factors that can influence the behavior of these short peptides. The aggregation kinetics of Aβ depends on the presence of metal ions,[10] lipids,[11] methionine-35 oxidation,[12] shaking,[13] salt concentration, temperature and pH.[14] Moreover, the presence of preformed aggregates and electrostatic surfaces can drastically promote fibrillation *in vitro*[15] As an example of the extreme variability of these assays, in Fig. 4 of the main text we showed a sample where the presence of a single piece of dust promoted the formation of a long macroscopic fibrillary aggregate into the NMR tube.

The presence of this impurity had a dramatic effect on the aggregation kinetics. Some fibril nuclei were formed on the surface of the dust particle in the bottom of the tube, where the macroscopic fibrillary aggregate started to grow. From these quickly formed aggregates the aggregation proceeded mainly through polymerization. This hypothesis is also in line with the observation of an exponential decay of the monomer signal (Fig.4A). Indeed, with reference to Eq. S6, a pure polymerization kinetics from a preformed concentration of fibrils (F_0) implies an exponential decay of the monomer ($m(t)$), considering a fixed monomer initial concentration (m_0)

$$\frac{dm(t)}{dt} \sim m_0 - k_+ F_0 m \;\rightarrow\; m(t) \sim Ae^{-k_+ F_0 t} + B \qquad \text{(S6)}$$

This curious example just highlights how complex is the problem of reproducibility on these samples, which requires working on extremely clean and freshly monomerized Aβ1-40. Despite all these attentions, the kinetics can sometimes follow slightly different trends depending on difficulties in carefully controlling all these variables. For example, the trends of the experimental monomer consumption measured for the Aβ1-40 50 μM in Fig. 2 and Fig. 3 are very similar but not superimposable. This could be due to the presence of ThT, but also to the difficulties to control the very small concentrations of impurities. For the above reasons, solution NMR is a profitable technique to follow these aggregation processes, because it gives an overview of the whole sample. In several cases, the presence of impurities in the sample or the concomitant occurrence of degradation processes (for example due to undetectable amounts of proteases)[16] can be determined by 1D ^{1}H NMR spectra (Fig. S10), NMR allows one to recognize a biased aggregation kinetics from a relevant one. Protein degradation can be prevented, at first instance, by obtaining an ultra-pure sample from the purification step. Then, we found that using EDTA (1.0 mM), protease inhibitors (Roche cOmplete™, EDTA-free Protease Inhibitor Cocktail, diluted 1:200) and sodium azide (0.2%) it is possible to block any form of bacterial contamination and residual proteases activity.

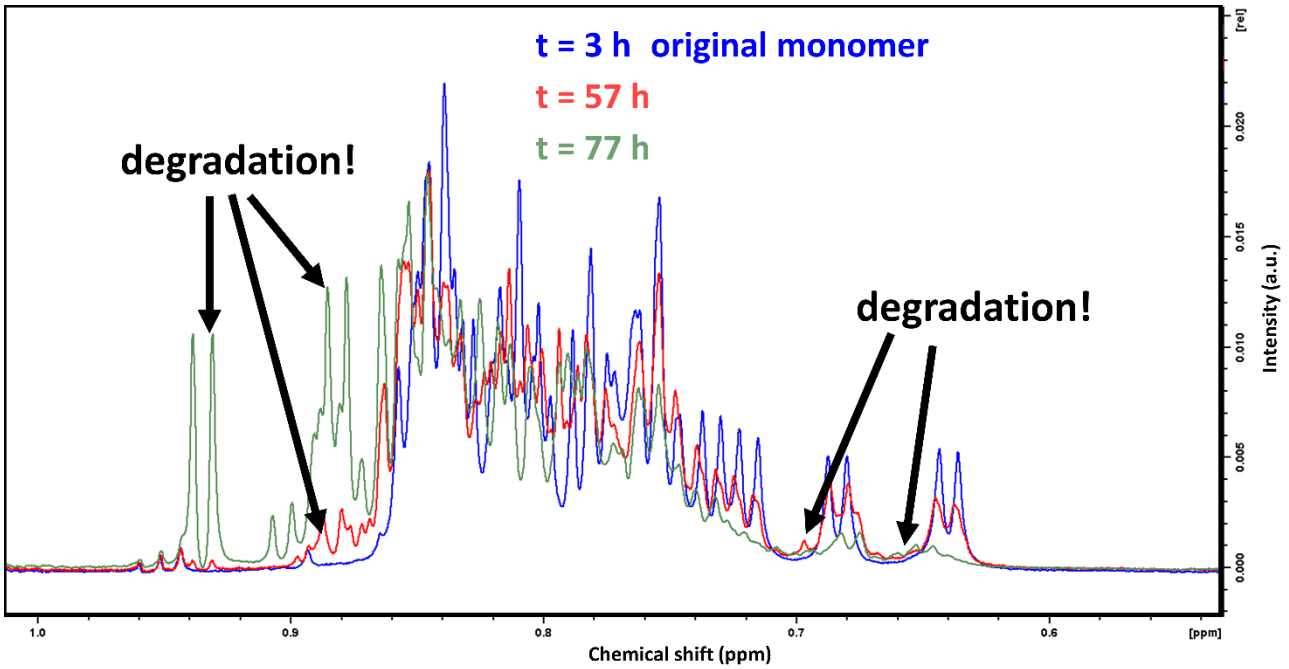

Figure S10: Spectra at different time points of a 40 µM Aβ1-40 sample at 298 K, pH 8.5 in ammonium acetate buffer in absence of EDTA, NaN_3 and protease inhibitors. The growth of sharp peaks near the monomer signals in the methyl region is a hallmark of degradation.

7. Experimental

7.1 AβM1-40 expression and purification

Escherichia Coli BL21(DE3) pLysS cells were transformed with pET-3a(+) vector containing the gene encoding the AβM1-40 peptide gene. The expression was performed using the Marley method.[17] Transformed cells were grown in LB medium until OD600 value reached 0.6-0.8 and, after a centrifugation at 3500 rpm (JA-10, Beckman Coulter), the pellet was exchanged into the M9 minimal medium containing $(^{15}NH_4)_2SO_4$ 1.0 g/L as sole nitrogen source. The same method was used to obtain unlabelled samples. The expression was induced with 1.2 mM Isopropyl-β-D-thiogalactoside and, after 4 hours incubation at 39 °C, cells were harvested at 4000 rpm (JA-10, Beckman Coulter). The pellet was suspended in TRIS 10mM, EDTA 1.0 mM, pH 8.0 buffer and sonicated for 40 minutes (cycle ON 2 seconds, cycle OFF 15 seconds). The suspension was utracentrifuged at 40000 rpm (Type 70 Ti rotor, Beckman Coulter) for 25 min and the pellet was collected, washed with TRIS 10 mM, EDTA 1.0 mM, pH 8.0 buffer and utracentrifuged a second time. Surnatant was discarded and, since Aβ peptides are expressed into inclusion bodies (IBs), a homogenization step with a buffer TRIS 10mM, EDTA 1.0 mM, pH 8.0 containing Urea 8.0 M, until the IBs were fully solubilized, was needed. Purification was performed through anion exchange chromatography in batch with TRIS 10 mM, EDTA 1.0 mM, NaCl 20 mM, 50 mM, 125 mM, 150 mM, 300 mM, 1.0 M at pH 8.0 as elution buffer[18] using DEAE 52 cellulose (DE52) resin. Fractions containing the protein were collected and added to Guanidine hydrochloride 6.0 M. A size-exclusion chromatography step was carried out exploiting the preparative column HiLoad 26/600 Superdex 75 pg with 50 mM $(NH_4)OAc$ pH 8.5 as final buffer [19]. The typical NMR sample conditions counted 30 µM to 100 µM AβM1-40 in 50 mM $(NH_4)OAc$, EDTA 1.0 mM, NaN3 0.2%, Thioflavin-T 5.0 µM (only for samples which were used in parallel with fluorescence), SigmaFast Protease Inhibitor Cocktail (the most abundant component was ABSF 10 µM), 10% D_2O at pH 8.5.

7.2 NMR experiments

Solution NMR experiment were acquired on an Avance III 950 MHz Bruker spectrometer and 700 MHz spectrometer both equipped with a $^1H/^{13}C/^{15}N$ triple resonance cryoprobe. 1D ^1H NMR spectra were acquired with standard direct excitation sequence with excitation sculpting water suppression[20] and a standard 1D NOESY sequence with water presaturation.[21] ^1H π/2 pulse was calibrated at 12.51 µs, 24576 complex points were acquired with an overall acquisition time of 1.95 s, each experiment was acquired accumulating 512 scans with a recycle delay of 1.0 s. Experiments were processed with 65536 complex points and an exponential window function of 0.3 Hz. All the 1D NMR experiments were run at 310 K while the 2D ones at 298 K using new and clean 5 mm glass tubes.

7.3 ThT fluorescence

Fluorescence experiments were performed in a Cary Eclipse fluorescence spectrophotometer (Agilent). The excitation wavelength was set to 450 nm, the emission wavelength to 485 nm and the temperature was kept at 310 K, with emission and excitation slits of 5 nm. ThT final concentration was 5 μM. Fluorescence intensity was recorded every 5 minutes in quiescent conditions. A quartz cuvette with a sample volume 550 μL was used. We preferred the use of a quartz cuvette instead of the more frequently used well plates because it is known that the water/air interface can promote aggregation.[22] In a NMR tube, the ratio between the exposed interface and the sample volume is, in general, smaller than the one of well plate (0.036 mm^{-1} for a typical 5 mm NMR-tube with 550 μL of sample and 0.15-0.14 mm^{-1} for a common flat bottom well with 250 μL of sample). In a quartz cuvette (10 mm x 2 mm) with a sample volume of 550 μL, the exposed interface/sample volume ratio is 0.036 mm^{-1}, equal to the value obtained for the NMR tube.

7.4 Kinetic analysis

Monomer simulated concentrations were compared with the integral values of methyl signals of the 1D spectra (0.67-1.0 ppm) or with the integrals of the signals of QD2 protons of H6, H13 and H14 and QE protons of Y10 of the aromatic regions of 1D-NOESY spectra (6.7-7.1 ppm). While NMR integrals were normalized by simply dividing by the highest value in the 1D series, the ThT fluorescence data were normalized to 1 minus the final plateau value (normalized integral) of the replicate sample in the NMR spectrometer. The kinetic simulations were performed by integrating with Euler method (total points 150000, discrete time interval = 2 s) the kinetic differential equations (Eq. 2 and Eq. 3) describing oligomer and fibril population. The squared differences between the normalized integrals of the methyl signals and the simulated monomer populations were minimized in parallel for different monomer concentrations by optimizing the kinetic constants using a Nelder-Mead minimization algorithm.[23]

7.5 HPLC-Mass Spectrometry

One aliquot of freshly purified and monomerized AβM1-40 (that is the peptide used in manuscript, which corresponds to the Aβ1-40 peptide with an additional methionine in the position 0, and is commonly named AβM1-40 in the text) was frozen (–80 °C) and successively checked by HPLC-MS in a HPLC Dionex Thermo instrument, model Ultimate 3000, coupled to a Thermo LTQ-Orbitrap mass spectrometer via ESI interface. The HPLC column was an Agilent Zorbax 300SB C8 2.1 x 100 mm, 3.5 μm. A gradient elution was performed with two solvents: solvent A H2O with 0.1% formic acid, and solvent B acetonitrile with 0.1% formic acid. The gradient started at time 0.00 minutes with 97% A and 3% of solvent B, reaching at 11.75 min 50% of B, and at time 14.75 min 20% of A and 80% of B. The flow rate was 0.40 mL/min and the injected sample volume was 5 μL. The Mass spectra of the eluted sample were continuously acquired with an Orbitrap system at resolution 30000 (at m/z = 400) in the range of m/z 300–2000. The ESI interface parameters were: Spray voltage 5 kV; Capillary voltage 10 V; Tube lens 60 V; Capillary temperature 280°C. Gas: Sheath gas 10 (arbitrary units), Auxiliary gas 5, Sweep gas 5.

Figure S11 reports the elution profile acquired for m/z comprised between 1000 and 1500. The main peak is composed by the monomeric AβM1-40 with high degree of purity. The figure S12 reports the mass distribution in the central region of the elution peak at times comprised between 8.15 min and 8.48 min. The main patterns, with charges z=4, 5, 6, 7, correspond to the multicharged AβM1-40 peptide. Figure S13 reports the enlarged region around m/z = 893 where is possible to see, together with the isotopic profile of the positive pentacharged AβM1-40 peptide, also the pentacharged isotopic pattern of a small amount of oxidized peptide ($MW_{A\beta M1-40} + {}^{16}O$), probably related to the oxidation of one of the two methionine residues, (either M0 or M35). Figure S14 reports the enlargement of the tetracharged peptide (m/z= 1116.06) where is possible to recognize also here a small amount of the oxidized peptide (m/z=1120.06) and of the peptide without the initial methionine (–131 uma) (m/z=1083.30). The relative amount of these impurities is estimated on the bases of the integrals of the multi charged patterns: the amount of oxidized peptide is of the order of 5.82% of the not oxidized AβM1-40, while the Aβ1-40 (missing the first methionine) is about 2.82% of the entire peptide.

While the presence, or the missing of the first methionine is expected to have almost no-influence in the aggregation kinetics,[18] the Aβ1-40 peptide fully oxidized at the methionine-35 shows large differences in the aggregation behaviour.[24,25] Nevertheless, since we are in presence of only a very small amount of oxidized species (that could be either M0 or M35) we expect this impurity has no influence in the observed aggregation kinetics.

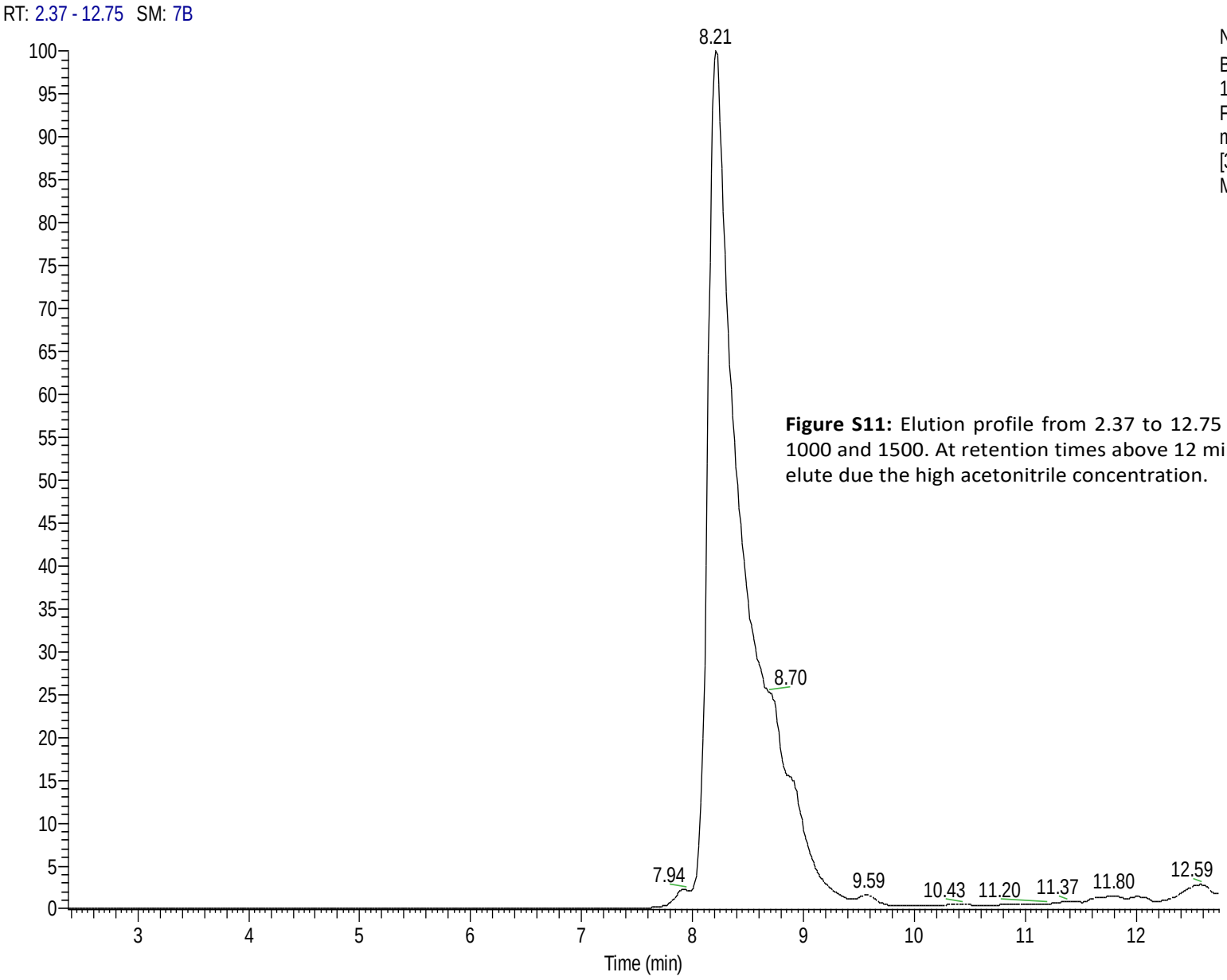

Figure S11: Elution profile from 2.37 to 12.75 min acquired at m/z between 1000 and 1500. At retention times above 12 min column impurities start to be elute due the high acetonitrile concentration.

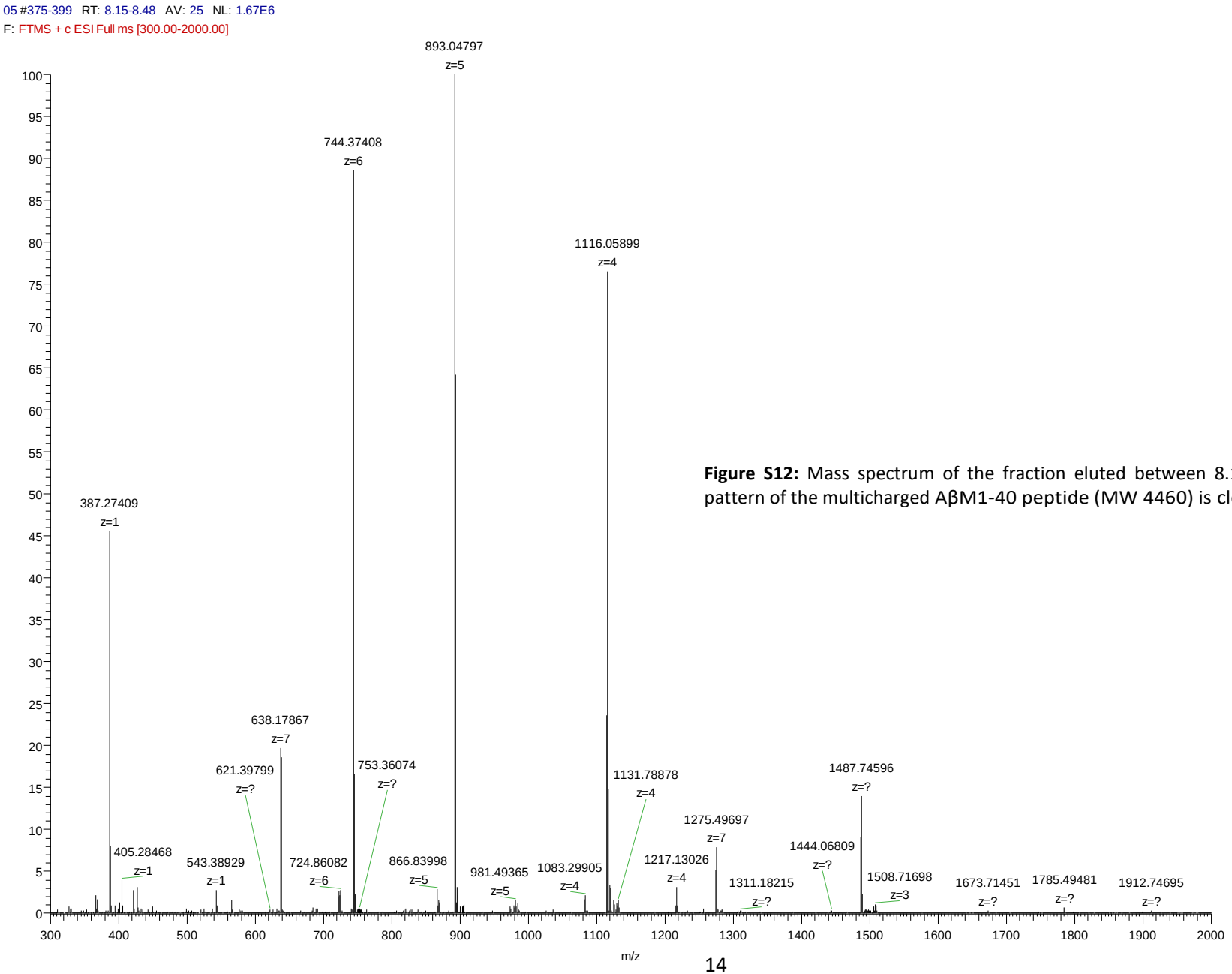

Figure S12: Mass spectrum of the fraction eluted between 8.15 and 8.48 min. The pattern of the multicharged AβM1-40 peptide (MW 4460) is clearly visible.

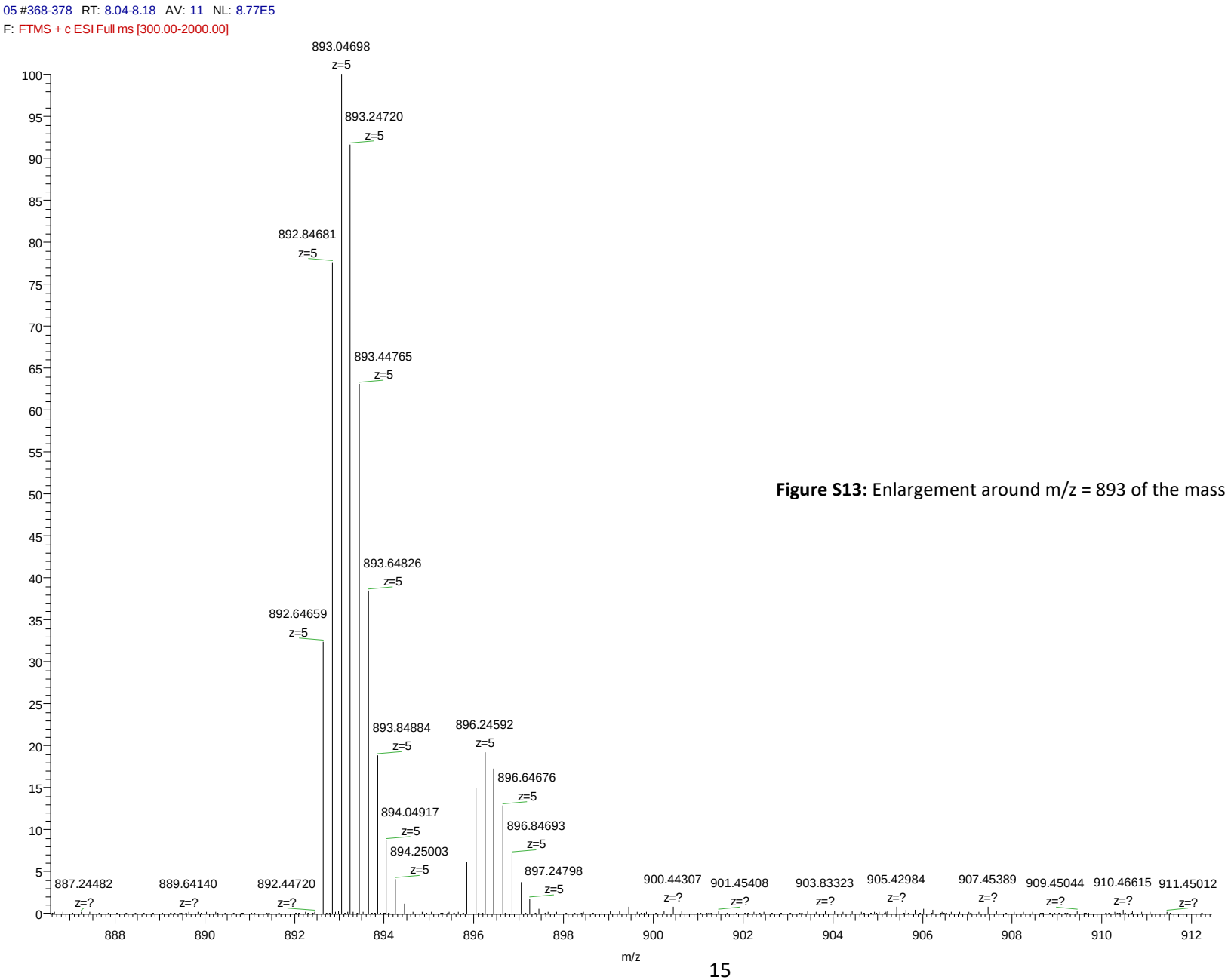

Figure S13: Enlargement around m/z = 893 of the mass spectrum of Figure S12.

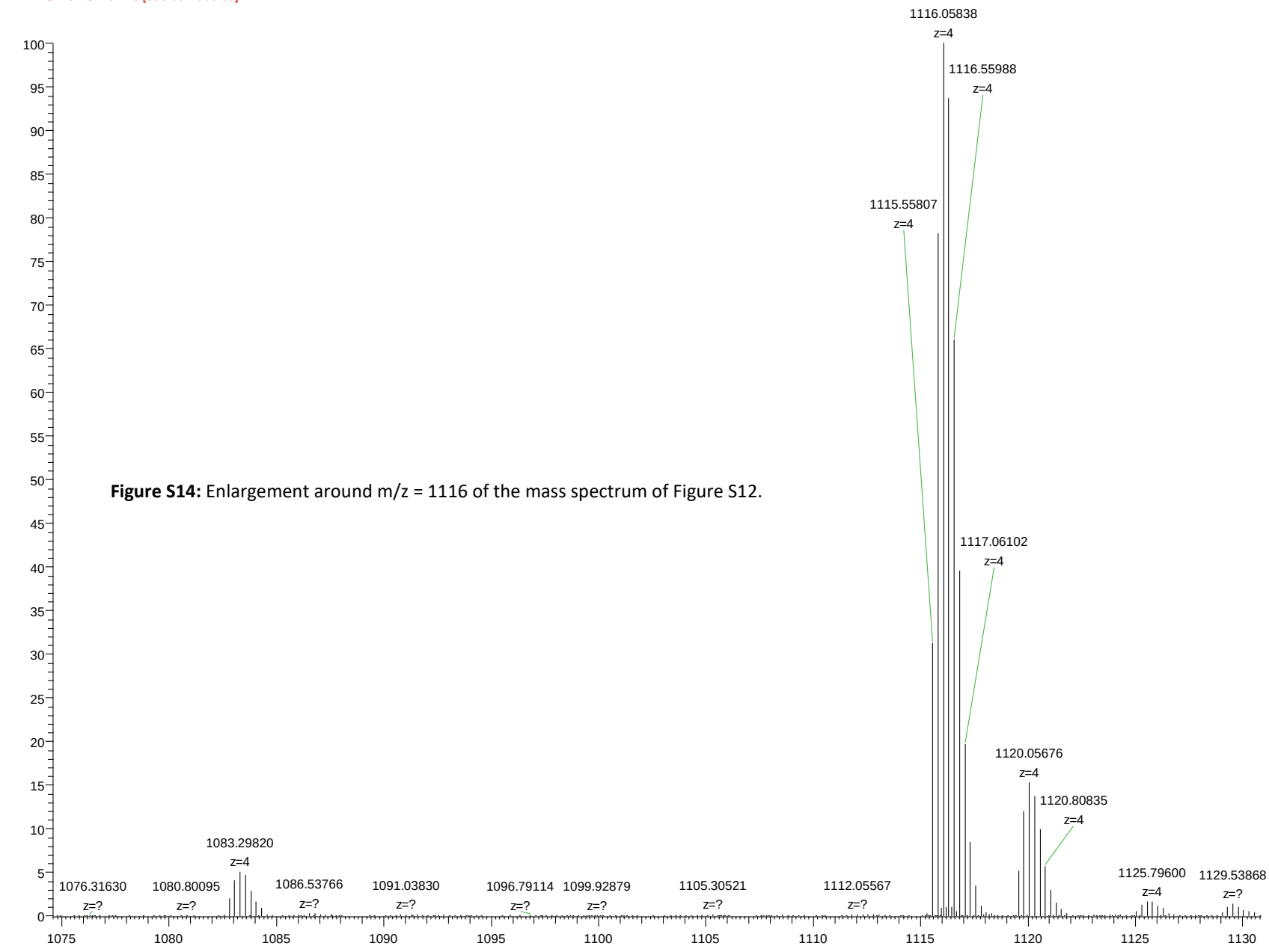

Figure S14: Enlargement around m/z = 1116 of the mass spectrum of Figure S12.

References

1 I. Bertini, G. Gallo, M. Korsak, C. Luchinat, J. Mao and E. Ravera, *Chembiochem Eur. J. Chem. Biol.*, 2013, **14**, 1891–1897.
2 S. I. A. Cohen, M. Vendruscolo, M. E. Welland, C. M. Dobson, E. M. Terentjev and T. P. J. Knowles, *J. Chem. Phys.*, 2011, **135**, 065105.
3 F. Ferrone, *Methods Enzymol.*, 1999, **309**, 256–274.
4 T. Pöschel, N. V. Brilliantov and C. Frömmel, *Biophys. J.*, 2003, **85**, 3460–3474.
5 F. Oosawa and M. Kasai, *J. Mol. Biol.*, 1962, **4**, 10–21.
6 S. I. A. Cohen, S. Linse, L. M. Luheshi, E. Hellstrand, D. A. White, L. Rajah, D. E. Otzen, M. Vendruscolo, C. M. Dobson and T. P. J. Knowles, *Proc. Natl. Acad. Sci.*, 2013, **110**, 9758–9763.
7 M. M. Pallitto and R. M. Murphy, *Biophys. J.*, 2001, **81**, 1805–1822.
8 G. Meisl, X. Yang, E. Hellstrand, B. Frohm, J. B. Kirkegaard, S. I. A. Cohen, C. M. Dobson, S. Linse and T. P. J. Knowles, *Proc. Natl. Acad. Sci. U. S. A.*, 2014, **111**, 9384–9389.
9 J. K. Davis and S. S. Sindi, *Appl. Math. Lett.*, 2015, **40**, 97–101.
10 F. Hane and Z. Leonenko, *Biomolecules*, 2014, **4**, 101–116.
11 M. Vestergaard, T. Hamada, M. Morita and M. Takagi, *Curr. Alzheimer Res.*, 2010, **7**, 262–270.
12 L. Hou, I. Kang, R. E. Marchant and M. G. Zagorski, *J. Biol. Chem.*, 2002, **277**, 40173–40176.
13 C. F. Lee, S. Bird, M. Shaw, L. Jean and D. J. Vaux, *J. Biol. Chem.*, 2012, **287**, 38006–38019.
14 B. Morel, L. Varela, A. I. Azuaga and F. Conejero-Lara, *Biophys. J.*, 2010, **99**, 3801–3810.
15 B. Moores, E. Drolle, S. J. Attwood, J. Simons and Z. Leonenko, *PLoS ONE*, , DOI:10.1371/journal.pone.0025954.
16 T. Saido and M. A. Leissring, *Cold Spring Harb. Perspect. Med.*, , DOI:10.1101/cshperspect.a006379.
17 J. Marley, M. Lu and C. Bracken, *J. Biomol. NMR*, 2001, **20**, 71–75.
18 D. M. Walsh, E. Thulin, A. M. Minogue, N. Gustavsson, E. Pang, D. B. Teplow and S. Linse, *FEBS J.*, 2009, **276**, 1266–1281.
19 I. Bertini, L. Gonnelli, C. Luchinat, J. Mao and A. Nesi, *J. Am. Chem. Soc.*, 2011, **133**, 16013–16022.
20 T. L. Hwang and A. J. Shaka, *J. Magn. Reson. A*, 1995, **112**, 275–279.
21 S. Bouatra, F. Aziat, R. Mandal, A. C. Guo, M. R. Wilson, C. Knox, T. C. Bjorndahl, R. Krishnamurthy, F. Saleem, P. Liu, Z. T. Dame, J. Poelzer, J. Huynh, F. S. Yallou, N. Psychogios, E. Dong, R. Bogumil, C. Roehring and D. S. Wishart, *PloS One*, 2013, **8**, e73076.
22 C. Schladitz, E. P. Vieira, H. Hermel and H. Möhwald, *Biophys. J.*, 1999, **77**, 3305–3310.
23 R. O'Neill, *J. R. Stat. Soc. Ser. C Appl. Stat.*, 1971, **20**, 338–345.
24 L. Hou, H. Shao, Y. Zhang, H. Li, N. K. Menon, E. B. Neuhaus, J. M. Brewer, I.-J. L. Byeon, D. G. Ray, M. P. Vitek, T. Iwashita, R. A. Makula, A. B. Przybyla and M. G. Zagorski, *J. Am. Chem. Soc.*, 2004, **126**, 1992–2005.
25 M. Friedemann, E. Helk, A. Tiiman, K. Zovo, P. Palumaa and V. Tõugu, *Biochem. Biophys. Rep.*, 2015, **3**, 94–99.